Electronic and Molecular Structure of High-Spin d^4 Complexes: Experimental and Theoretical Study of the [Cr(D$_2$O)$_6$]$^{2+}$ Cation in Tutton's Salts

Christopher Dobe,† Christopher Noble,† Graham Carver,†
Philip L. W. Tregenna-Piggott,*,† Garry J. McIntyre,‡ Anne-Laure Barra,§
Antonia Neels,¶ Stefan Janssen,# and Fanni Juranyi#,&

*Contribution from the Department of Chemistry and Biochemistry, University of Bern,
Freiestrasse 3, CH-3000, Bern 9, Switzerland, Institut Laue-Langevin, BP156, 38043,
Grenoble Cedex 9, France, High Magnetic Field Laboratory, CNRS/MPI, B.P. 166,
38042 Grenoble, France, Institut de Chimie, Université de Neuchâtel, Avenue de Bellevaux 51,
C.P. 2, CH-2007 Neuchâtel, Switzerland, Laboratory for Neutron Scattering, PSI,
CH-5232 Villigen, Switzerland, and Department of Physical Chemistry, Saarland University,
D-66123 Saarbrücken, Switzerland*

Received July 1, 2004; E-mail: tregenna@iac.unibe.ch

Abstract: Variable-temperature spectroscopic and crystallographic studies on the chromium(II) Tutton's salts, (M^I)$_2$Cr(X$_2$O)$_6$(SO$_4$)$_2$, where M^I = ND$_4^+$, Rb$^+$, or Cs$^+$, and X = H or D, are reported. Inelastic neutron scattering (INS) and multifrequency EPR experiments facilitate a rigorous definition of the ground-state electronic structure from 1.5 up to 296 K, which is unprecedented for a high-spin d^4 complex. Modeling of the INS data using a conventional $S = 2$ spin Hamiltonian reveals a dramatic variation in the axial and rhombic zero-field-splitting parameters. For the ammonium salt, D and E are $-2.454(3)$ and $0.087(3)$ cm^{-1} at 10 K and $-2.29(2)$ and $0.16(3)$ cm^{-1} at 250 K, respectively. A temperature variation in the stereochemistry of the [Cr(D$_2$O)$_6$]$^{2+}$ complex is also identified, with an apparent coalescence of the long and medium Cr$-$O bond lengths at temperatures above 150 K. The corresponding changes for the rubidium and cesium salts are notable, though less pronounced. The experimental quantities are interpreted using a ^{5}E⊗e Jahn$-$Teller Hamiltonian, perturbed by anisotropic strain. It is shown that good agreement can be obtained only by employing a model in which the anisotropic strain is itself temperature dependent. A new theoretical approach for calculating variable-temperature EPR spectra of high-spin d^4 complexes, developed within the ^{5}E⊗e coupling model, is described. Differences between spin-Hamiltonian parameters determined by INS and EPR are consistent with those of the different time scales of the two techniques.

1. Introduction

The theoretical description of integer-spin complexes has received new impetus following the recent abundance of spectroscopic data. High-field, multifrequency electron paramagnetic resonance (HFEPR),[1] inelastic neutron scattering (INS),[2] far-infrared spectroscopy (FIR),[3] and magnetic circular dichroism (MCD)[4] have all been used to probe the low-energy electronic structure of non-Kramers ions, with octahedrally

coordinated high-spin d^4 complexes receiving particular attention.[2,5-9] Measurements of the electronic structure are commonly confined to temperatures well below that of liquid nitrogen, and the determined zero-field-splitting (zfs) parameters then are related to the room temperature molecular geometry through a conventional ligand-field model. This approach cannot be considered wholly correct, however, given that a strong temperature dependence of the experimental quantities can arise from dynamical Jahn$-$Teller coupling. This work demonstrates the profound influence of dynamical effects on the electronic and molecular structrure of octahedrally coordinated high-spin d^4 complexes. Experimental data are presented that define a pronounced variation in the spin-Hamiltonian parameters and

---

† University of Bern.
‡ Institut Laue-Langevin.
§ CNRS/MPI.
¶ Université de Neuchâtel.
# Laboratory for Neutron Scattering.
& Saarland University.

(1) Smith, G. M.; Riedi, P. C. *Electron Paramagn. Reson.* **2000**, *17*, 164−204.
(2) Basler, R.; Tregenna-Piggott, P. L. W.; Andres, H.; Dobe, C.; Gudel, H.; Janssen, S.; McIntyre, G. J. *J. Am. Chem. Soc.* **2001**, *123*, 3377−3378.
(3) Vongtragool, S.; Gorshunov, B.; Dressel, M.; Krzystek, J.; Eichhorn, D. M.; Telser, J. *Inorg. Chem.* **2003**, *42*, 1788−1790.
(4) Pavel, E. G.; Solomon, E. I. Recent Advances in Magnetic Circular Dichroism Spectroscopy. In *Spectroscopic Methods in Bioinorganic Chemistry*; Solomon, E. I., Hodgson, K. O., Eds.; ACS Symposium Series 692; American Chemical Society: Washington, DC, 1998; pp 119−135.

(5) Gatteschi, D.; Sorace, L.; Sessoli, R.; Barra, A. L. *Appl. Magn. Reson.* **2001**, *21*, 299−310.
(6) Krzystek, J.; Yeagle, G. J.; Park, J.-H.; Britt, R. D.; Meisel, M. W.; Brunel, L.-C.; Telser, J. *Inorg. Chem.* **2003**, *42*, 4610.
(7) Telser, J.; Pardi, L. A.; Krzystek, J.; Brunel, L.-C. *Inorg. Chem.* **1998**, *37*, 5769.
(8) Telser, J.; Pardi, L. A.; Krzystek, J.; Brunel, L.-C. *Inorg. Chem.* **2000**, *39*, 1834.
(9) Dobe, C.; Andres, H.; Tregenna-Piggott, P.; Mossin, S.; Weihe, H.; Janssen, S. *Chem. Phys. Lett.* **2002**, *362*, 387.

---

metal−ligand bond lengths with temperature, requiring a theoretical approach that goes beyond the conventional ligand-field model to include the vibrational coordinates of the molecule.

An experimental and theoretical study of the $[Cr(OX_2)_6]^{2+}$ complex, within the chromium(II) Tutton's salts of formula $(M^I)_2[Cr(OX_2)_6](SO_4)_2$, where $M^I = NH_4^+$, Rb^+, or Cs^+ and X = D or H, is presented. Complexes of chromium(II) are prone to oxidation and have been subject to far fewer experimental studies than their isoelectronic manganese(III) counterparts. This crystal series was chosen since the copper(II) analogues exhibit properties indicative of the effects of dynamical Jahn−Teller coupling that we wish to examine in high-spin d^4 complexes.

Previous structural studies of chromium(II) Tutton's salts have been limited to the ammonium salt. Unlike hydrogenous ammonium copper sulfate, there is no structural change on deuteration, with both chromium salts adopting the deuterated ammonium copper sulfate form.[10] Single-crystal X-ray and neutron studies at 298,[11,12] 84,[13] and 4.2[14] K suggest an apparent contraction of the long bond and lengthening of the intermediate bond length as the temperature is raised, mirroring the fluxional behavior observed in the copper analogues.[15,16] Several structural studies have also been performed on the related hexafluorosilicate compound,[17] revealing a fully dynamic structure at room temperature. EXAFS carried out on the $[Cr(H_2O)_6]^{2+}$ cation in solution[18] suggested particularly loose axial coordination of the water molecules.

Electronic spectroscopic studies of Cr(II) Tutton's salts have been confined to room temperature optical reflectance measurements of the NH_4^+, Rb^+, and Cs^+ salts.[19] The spectra were interpreted along with magnetic data using a conventional ligand-field model.[20] Detailed analysis and assignments of chromium(II) optical spectra have also been carried out for many other simple inorganic compounds.[21−23]

The first reported EPR measurement on a chromium(II) compound was a negative result at X-band on $(NH_4)_2Cr(H_2O)_6$-$(SO_4)_2$.[24] After this study, room temperature single-crystal EPR spectra were obtained on $CrSO_4 \cdot 5H_2O$ at frequencies between 27 and 55 GHz.[25,26] Later studies focused on conventional frequencies with chromium(II) as a dopant in semiconductor lattices.[27,28] The most comprehensive HFEPR study to date has been on the chromium(II) cation in an aqueous glass by Telser et al.,[7,8] from which the *D* tensor of the $[Cr(H_2O)_6]^{2+}$ cation

was found to be axially symmetric and a regular tetragonal CrO_6 framework inferred.

The foregoing physical techniques are all employed in the present study, but the measurements undertaken are over a wide temperature range, facilitating a rigorous definition of the electronic and molecular structure. Presented for the first time are good-quality, high-field, high-frequency EPR spectra for a pure, "not-so-EPR-silent" monomeric chromium(II) compound. A theoretical model is described, relating the resonance positions to the plasticity of the coordination sphere and the interstate relaxation rate. The foremost spectroscopic tool utilized is INS, which affords the direct determination of the ground-state electronic structure at zero field over a wide temperature range. Preliminary INS spectra, recorded for the ammonium salt, have been communicated previously.[9]

The crystallographic and spectroscopic data are modeled using a vibronically coupled $^5E \otimes e$ Hamiltonian in an extension to that used successfully to interpret the temperature-dependent properties of the copper(II) Tutton's salts.[16,29] The marked temperature dependence of the bond lengths and zfs parameters of the $[Cr(H_2O)_6]^{2+}$ complex can be modeled within a consistent framework, but only by assuming that the ligand-field is itself temperature dependent. Furthermore, we show that the experimentally determined zfs parameters depend strongly on the time scale of the experimental technique.

2. Experimental Section

2.1. Synthesis. All deuterated products were handled under a nitrogen atmosphere to prevent exchange with atmospheric water; all chromium(II) compounds were prepared with the rigorous exclusion of oxygen using standard Schlenk techniques. $(ND_4)_2SO_4$ was prepared by multiple recrystallizations of the hydrogenous salt from boiling D_2O. $CrSO_4 \cdot 5D_2O$ was prepared by refluxing (100 °C) electrolytic chromium metal (5 g, 99.99%, Provac) with D_2O (50 mL, 99.8% D, Armar) and concentrated D_2SO_4 (10 mL, 99.5% D, Armar). The resulting bright-blue solution was filtered while hot and allowed to cool slowly to room temperature before being further cooled to 2 °C overnight. The blue crystals were filtered and dried under a flow of nitrogen gas. $(ND_4)_2Cr(D_2O)_6(SO_4)_2$ was prepared by combining the starting materials in equimolar quantities, followed by the addition of a minimum quantity of D_2O, and then heating until dissolution; crystals formed on slow cooling.

The $Rb_2Cr(D_2O)_6(SO_4)_2$ and $Cs_2Cr(H_2O)_6(SO_4)_2$ analogues were synthesized by the combination of solutions containing $CrSO_4 \cdot 5D_2O$ with either Rb_2SO_4 (99%, Alfa Aesar) or Cs_2SO_4 (99.9%, Alfa Aesar), using a procedure analagous to that described above. The cesium salt was found to be problematic, easily dehydrating to the dihydrate[19] (bright purple in color), necessitating rapid handling during synthesis and in the glovebox. Powder X-ray diffraction was used to confirm the structure and purity of all the compounds. Hydrogenous salts were prepared by the same procedure, with hydrogenous starting materials. Single-crystals were grown by slow cooling of warm, saturated solutions.

2.2. Inelastic Neutron Scattering Measurements. Time-of-flight INS measurements were carried out on FOCUS[30] at the Paul Scherrer Institute (PSI) (Villigen, Switzerland). Deuterated samples were lightly ground, placed in standard aluminum sample holders (cylindrical, 10

(10) Henning, R. W.; Schultz, A. J.; Hitchman, M. A.; Kelly, G.; Astley, T. *Inorg. Chem.* **2000**, *39*, 765.
(11) Cotton, F. A.; Daniels, L. M.; Murillo, C. A.; Quesada, J. F. *Inorg. Chem.* **1993**, *32*, 4861.
(12) Araya, M. A.; Cotton, F. A.; Daniels, L. M.; Falvello, L. R.; Murillo, C. A. *Inorg. Chem.* **1993**, *32*, 4853.
(13) Figgis, B. N.; Kucharski, E. S.; Reynolds, P. A. *Acta Crystallogr.* **1990**, *B46*, 577.
(14) Figgis, B. N.; Kucharski, E. S. *Acta Crystallogr.* **1991**, *C47*, 419.
(15) Hathaway, B. J.; Hewat, A. W. *J. Solid State Chem.* **1984**, *51*, 364.
(16) Riley, M. J.; Hitchman, M. A.; Mohammed, A. W. *J. Chem. Phys.* **1987**, *87*, 3766.
(17) Cotton, F. A.; Falvello, L. R.; Murillo, C. A.; Quesada, J. F. *J. Solid State Chem.* **1992**, *96*, 192.
(18) Sham, T. K.; Hastings, J. B.; Perlman, M. L. *Chem. Phys. Lett.* **1981**, *83*, 391.
(19) Earnshaw, A.; Larkworthy, L. F.; Patel, K. C.; Beech, G. *J. Chem. Soc. A* **1969**, 1334.
(20) Earnshaw, A.; Larkworthy, L. F.; Patel, K. C. *Chem. Commun.* **1966**, *7*, 181.
(21) Fackler, J. P.; Holah, D. G. *Inorg. Chem.* **1965**, *4*, 954.
(22) Runciman, W. A.; Syme, R. W. G. *Philos. Mag.* **1963**, *8*, 605.
(23) Lim, P. E.; Stout, J. W. *J. Chem. Phys.* **1975**, *63*, 4886.
(24) Abragam, A.; Pryce, M. H. L. *Proc. R. Soc. A* **1951**, *205*, 142.
(25) Ono, K.; Koide, S.; Sekiyama, H.; Abe, H. *Phys. Rev.* **1954**, *96*, 38.
(26) Ono, K. *J. Phys. Soc. Jpn.* **1957**, *12*, 1231.

(27) Jablonski, R. *Mater. Res. Bull.* **1973**, *8*, 909.
(28) Boonman, M.; Mac, W.; Twardowski, A.; Wittlin, A.; van Bentum, P. J. M.; Maan, J. C. *Phys. Rev. B* **2000**, *61*, 5358.
(29) Masters, V. M.; Riley, M. J.; Hitchman, M. A. *Inorg. Chem.* **2001**, *40*, 843.
(30) Mesot, J.; Janssen, S.; Holitzner, L.; Hempelmann, R. *J. Neutron Res.* **1996**, *3*, 293.

Table 1. Summary of Neutron DIffraction Crystal Data and Refinements

chemical formula	$(NH_4)_2Cr(H_2O)_6(SO_4)_2$
formula weight	388.2 g/mol
cell setting	monoclinic
space group	$P2_1/a$
wavelength	1.0–2.2 Å
Z	2
crystal form	tabloid
crystal size	$2.5 \times 3.0 \times 0.5$ mm³
crystal color	light blue
refinement on	F
weighting scheme	$W = 1/[\max(\sigma^2(F_o^2), \sigma_{pop}(F_o^2)]$
extinction method	Lorentzian type 1 isotropic[a]
atomic scattering factors	Sears[b]
No. params in refinement	179

[a] From refs 36 and 37. *[b]* From ref 38.

mm diameter × 50 mm length), and sealed under a helium atmosphere. An incident wavelength of 5.3 Å was selected, yielding an energy transfer window extending to +15 cm⁻¹. The energy resolution was optimized for an energy transfer of 0 cm⁻¹ (elastic time focusing) for maximum resolution of the elastic peak. For the 297 K measurement, the cryostat (standard ILL Orange Cryostat) was removed and the sample mounted directly in the sample space. The detectors were calibrated with a vanadium metal spectrum and standard background corrections applied using the Nathan software, developed at PSI. A correction for detector efficiency was also applied.

2.3. Structural Data Collection. Single-crystal neutron diffraction was performed on the new quasi-Laue diffractometer, VIVALDI,[31] at the ILL (Grenoble, France). VIVALDI uses the Laue diffraction method on an unmonochromated thermal-neutron beam with a large solid angle (8 sterad) cylindrical image-plate detector to increase the detected diffracted intensity by 1–2 orders of magnitude compared with that of a conventional monochromatic experiment. The single-crystal of $(NH_4)_2$-$Cr(H_2O)_6(SO_4)_2$ ($2.5 \times 3.0 \times 0.5$ mm³) was mounted in thin aluminum foil on an aluminum pin with epoxy cement. The image-plate Laue data were indexed with Lauegen.[32] The 10 K data consisted of eight Laue diffraction patterns distinguished by 20° rotations of the crystal about the vertical axis of the cylindrical detector. Higher temperature data utilized four patterns separated by 40°. Exposure times were 90 min per pattern. Integration was performed using the local program, Argonne-Boxes,[33] which uses a two-dimensional version of the 3D σ-$(I)/I$ algorithm. The individual reflections were corrected for absorption using the calculated (wavelength-dependent) attenuation coefficient $0.104 \lambda + 0.125$ mm⁻¹ (transmission range 0.50–0.89). Multiple patterns were combined and normalized to the same incident wavelength with Lauenorm,[34] and the full data set were refined from initial literature values using SFLSQ (CCSL).[35] There were 179 parameters refined at each temperature and they included a scale factor, an isotropic extinction parameter, positional parameters, and anisotropic thermal displacement parameters for all atoms. Some of the second-order displacement tensors became slightly nonpositive, which we attribute to the sparser sampling of reciprocal space along the crystal rotation axis. The variation of the Cr–O bond lengths with temperature was, however, more regular when anisotropic displacement tensors were refined, and our discussion of the Cr–O bond lengths is based on these refinements. The collected data are summarized in Tables 1 and 2.

VIVALDI utilizes a white neutron beam; the unit-cell parameters cannot be determined accurately, necessitating the collection of

additional data. Powder X-ray diffraction (PXRD) measurements were performed on a STOE STADI P diffractometer, in transmission mode, fitted with an Oxford Instruments Series 600 Cryostream Cooler. The finely ground sample was sealed in a 0.3 mm glass capillary, and diffractograms were obtained in the range $2\theta = 10$–$50°$ at temperatures corresponding to the VIVALDI data, down to 100 K. The unit-cell lengths were refined in the space group $P2_1/a$ using whole pattern refinement in FULLPROF.[39]

Single-crystal X-ray diffraction measurements were carried out by the BENEFRI Crystallography Service (Neuchâtel, Switzerland). Single crystals of $Rb_2Cr(H_2O)_6(SO_4)_2$ and $Cs_2Cr(H_2O)_6(SO_4)_2$ were placed in glass capillaries and data collected on a Stoe Mark II Image-Plate Diffraction System[40] using graphite-monochromated Mo Kα radiation, with an image-plate distance of 100 mm, ω oscillation scans of 0–180° at $\phi = 0°$, ω oscillation scans of 0–180° at $\phi = 90°$, step $\Delta\omega = 2°$, 2 min per exposure, 2θ range of 2.29–59.53°, and $d_{max} - d_{min} = 17.799$–$0.716$ Å. Data were collected at 100(2) and 293(2) K. The structures were solved by direct methods using the SHELXS-97[41] program and refined by full matrix least-squares on F^2 with SHELXL-97.[42] The positions of the hydrogen atoms were localized from Fourier difference maps and fixed in their positions. An empirical absorption correction was applied using DIFABS in PLATON99.[43] Crystal and refinement data are reported in Table 3.

2.4. EPR Measurements. High-field, high-frequency EPR data were collected at the Grenoble High Magnetic Field Laboratory (Grenoble, France). The apparatus has been described in detail previously.[44] Measurements were performed on the hydrogenous and deuterated ammonium salt, as well as on the hydrogenous rubidium salt, at frequencies ranging from 95 to 285 GHz. A small quantity of material was meticulously ground in a nitrogen-filled glovebox and mixed with an equal quantity of *n*-eicosane wax (mp = 36 °C, 95%; Fluka). A 4 mm diameter quartz tube was loaded to a depth of approximately 15 mm and sealed at a height of 100 mm under a helium atmosphere. Immersion of the tube in warm water melted the wax and, when cooled, formed a 10 × 4 mm solid, pale-blue pellet.

EPR spectra were recorded at X-band (~9.6 GHz) and Q-band (~35 GHz) with a Bruker ELEXSYS E500 spectrometer at the Department of Chemistry, University of Bern, Switzerland. X-band measurements were carried out utilizing an ER4122 SHQ or ER4116 DM cavity in conjunction with an Oxford Instruments ESR910 continuous flow cryostat (liquid helium temperatures) or with a BVT3000 cryostat (liquid nitrogen temperatures). The ER5106 Q-band cavity was fitted with an Oxford Instruments CF935 continuous flow helium cryostat and monitored with an HP53152A microwave frequency counter. The samples were ground in a glovebox and sealed in quartz tubes under a helium atmosphere.

EPR simulations were calculated using the software of Weihe[45] by full diagonalization of the $S = 2$ spin Hamiltonian matrix. Parameter optimizations were made using a brute-force, least-squares-based script.

2.5. Optical Absorption Measurements. A Cary 5e spectrometer was used to collect UV/vis/NIR spectra. Crystals of $(NH_4)_2Cr(H_2O)_6$-$(SO_4)_2$ and the deuterated analogue were polished in several stages down to a 0.5 μm grit. The unoriented crystals were then mounted, using

(31) Wilkinson, C.; Cowan, J. A.; Myles, D. A. A.; Cipriani, F.; Mcintyre, G. J. *Neutron News* **2002**, *13*, 37.
(32) Campbell, J. W.; Hao, Q.; Harding, M. M.; Nguti, N. N.; Wilkinson, C. *J. Appl. Crystallogr.* **1998**, *31*, 496.
(33) Wilkinson, C.; Khamis, H. W.; Stansfield, R. F. D.; McIntyre, G. J. *J. Appl. Crystallogr.* **1988**, *21*, 471.
(34) Campbell, J.; Habash, J.; Helliwell, J. R.; Moffat, K. *Protein Crystallogr.* **1986**, *18*, 23.
(35) Matthewman, J. C.; Thompson, P.; Brown, P. J. *J. Appl. Crystallogr.* **1982**, *15*, 167.

(36) Becker, P.; Coppens, P. *Acta Crystallogr.* **1974**, *A30*, 129.
(37) Becker, P.; Coppens, P. *Acta Crystallogr.* **1975**, *A31*, 417.
(38) Sears, V. F. *Methods Exp. Phys.* **1986**, *23A*, 521.
(39) Rodriguez-Carvajal, J. *FULLPROF*, version 2.00, Nov2001-LLB, unpublished.
(40) *X-Area V1.17 and X-RED32 V1.04 Software*; Stoe & Cie, GmbH: Darmstadt, Germany.
(41) Sheldrick, G. M. *Acta Crystallogr. A46*, 467–273.
(42) Sheldrick, G. M. *SHELXL-97: Program for Crystal Structure Refinement*; University of Göttingen: Göttingen, Germany, 1997.
(43) Spek, A. L. *Acta Crystallogr.* **1990**, *A46*, C34.
(44) Muller, F.; Hopkins, A.; Coron, N.; Grynberg, M.; Brunel, L. C.; Martinez, G. *Rev. Sci. Instrum.* **1989**, *60*, 3681. (b) Barra, A. L.; Brunel, L. C.; Robert, J. B. *Chem. Phys. Lett.* **1990**, *165*, 107.
(45) Glerup, J.; Weihe, H. *Acta Chem. Scand.* **1991**, 444.

Table 2. Single-Crystal Neutron Diffraction Data Collection and Analysis Parameters for $(NH_4)_2Cr(H_2O)_6(SO_4)_2$

temperature	10	100	150	200	225	250	275	300
No. patterns	8	4 (+2 repeats)	4	4	4	4	4	4
step size (deg)	20	40	40	40	40	40	40	40
unit cell								
a (Å)[b]	9.490(2)[a]	9.4721(9)	9.4723(9)	9.4696(8)	9.4514(9)	9.4525(5)	9.4436)4	9.4226(5)
b (Å)[b]	12.816(4)	12.8075(11)	12.8077(11)	12.8002(13)	12.7995(11)	12.7669(7)	12.7420(7)	12.6963(7)
c (Å)[b]	6.104(1)	6.1058(5)	6.1140(6)	6.1277(7)	6.1444(7)	6.1476(3)	6.1707(3)	6.2015(3)
β (deg)[b]	107.09(2)	107.049(4)	107.025(4)	106.908(5)	106.883(4)	106.816(3)	106.722(2)	106.595(3)
V (Å³)[b]	710(1)	708.2(1)	709.3(1)	710.6(1)	711.3(1)	710.15(7)	711.11(1)	711.00(6)
bragg R_f[b]		4.78	4.09	3.33	3.91	2.11	2.05	2.33
χ^2[b]		6.32	6.92	9.31	8.42	4.26	3.24	6.32
No. reflns (all)	6032	4268	2549	2629	2417	2340	2051	1825
No. independent reflns	1747	1490	1241	1284	1193	1165	970	885
R_{int}	0.136	0.097	0.110	0.116	0.106	0.111	0.118	0.094
h range	$-8 \leq h \leq 10$	$-7 \leq h \leq 10$	$-7 \leq h \leq 10$	$-7 \leq h \leq 10$	$-7 \leq h \leq 9$	$-7 \leq h \leq 9$	$-7 \leq h \leq 9$	$-7 \leq h \leq 8$
k range	$-20 \leq k \leq 14$	$-10 \leq k \leq 20$	$-10 \leq k \leq 18$	$-10 \leq k \leq 18$	$-10 \leq k \leq 18$	$-10 \leq k \leq 18$	$-10 \leq k \leq 16$	$-9 \leq k \leq 14$
l range	$-9 \leq l \leq 9$	$-9 \leq l \leq 9$	$-9 \leq l \leq 8$	$-9 \leq l \leq 8$	$-9 \leq l \leq 7$	$-9 \leq l \leq 8$	$-8 \leq l \leq 7$	$-7 \leq l \leq 6$
R(F)	0.117	0.106	0.112	0.119	0.109	0.113	0.115	0.106
wR(F)	0.089	0.072	0.072	0.080	0.074	0.075	0.084	0.080
χ^2	6.21	4.89	4.51	6.13	5.49	5.33	7.07	8.05
mosaic spread	0.1179	0.0660	0.0660	0.0660	0.0660	0.0660	0.0660	0.0660

[a] Unit cell parameters taken from ref 13. [b] From full pattern profile fitting of X-ray powder diffraction data in FULLPROF.

copper grease, in a home-built copper cell under helium gas. The cell was placed on the coldfinger of an Air Products closed-cycle refrigerator, and spectra were recorded as a function of temperature.

3. Theory

3.1. The Vibronic Hamiltonian. The crystallographic and spectroscopic data for the copper(II) Tutton's salts have been satisfactorily interpreted in terms of a cubic vibronic Hamiltonian, perturbed by low-symmetry strain.[16] An analogous approach is adopted here, employing an effective cubic ^5E_g electronic basis, generated by Mossin and Weihe,[9] using second-order perturbation theory.

The Hamiltonian for the problem is written as the sum

$$\hat{H} = \hat{H}_{cub} + \hat{H}_{st} + \hat{H}_{ph} + \hat{H}_{JT} \tag{1}$$

where $\hat{H}_{cub}$ and $\hat{H}_{st}$ designate the cubic and low-symmetry (strain) ligand-field contributions to the energy, respectively, and $\hat{H}_{ph}$ and $\hat{H}_{JT}$ are the phonon and Jahn–Teller coupling terms, respectively.

The following electronic operators are defined using the Clebsch–Gordan coefficients as tabulated by Sugano, Tanabe, and Kamimura (ref 46, p 305), operating in the θ, ϵ orbital basis of the ^5E_g ground term of the Cr(II) complex:

$$\hat{U}_\tau = \begin{pmatrix} 1 & 0 \\ 0 & 1 \end{pmatrix}, \hat{U}_\theta = \begin{pmatrix} -1 & 0 \\ 0 & 1 \end{pmatrix}, \hat{U}_\epsilon = \begin{pmatrix} 0 & 1 \\ 1 & 0 \end{pmatrix} \tag{2}$$

Note that the electronic operators in eq 2 differ in phase to those employed by Riley et al.[16] Comparison of our Hamiltonian to that defined by Riley et al. shows that the parameters A_1 and e_θ, defined below, should be multiplied by -1 in order to be consistent.

Only phonons of e_g symmetry are Jahn–Teller active in this basis, and the coupling is dominated by the $\nu_2(CrO_6)$ vibration, having the two components $Q_\theta \sim 2\Delta z^2 - \Delta x^2 - \Delta y^2$ and $Q_\epsilon \sim \sqrt{3}(\Delta x^2 - \Delta y^2)$, where x, y, and z denote the Cartesian

coordinates with respect to the 4-fold axes. $\hat{H}_{ph}$, the Hamiltonian for an e_g phonon mode before coupling, can be written as

$$\hat{H}_{ph} = [0.5\hbar\omega(\hat{P}_\theta{}^2 + \hat{P}_\epsilon{}^2 + \hat{Q}_\theta{}^2 + \hat{Q}_\epsilon{}^2) + A_3(3\hat{Q}_\theta\hat{Q}_\epsilon{}^2 - \hat{Q}_\theta{}^3)]\hat{U}_\tau \tag{3}$$

where $\hbar\omega$ is the phonon energy and A_3 the anharmonic constant. $\hat{Q}_i$ and $\hat{P}_i$ are dimensionless operators related to the observables for position and momentum, $\hat{q}_i$ and $\hat{p}_i$, by[47]

$$\hat{Q}_i = \sqrt{\frac{\mu\omega}{\hbar}}\hat{q}_i,$$

$$\hat{P}_i = \frac{1}{\sqrt{\mu\hbar\omega}}\hat{p}_i \tag{4}$$

where μ is the reduced mass of the phonon mode.

To second order, $\hat{H}_{JT}$ has the form

$$\hat{H}_{JT} = A_1(\hat{Q}_\theta\hat{U}_\theta + \hat{Q}_\epsilon\hat{U}_\epsilon) + A_2((\hat{Q}_\epsilon{}^2 - \hat{Q}_\theta{}^2)\hat{U}_\theta + 2\hat{Q}_\theta\hat{Q}_\epsilon\hat{U}_\epsilon) \tag{5}$$

where A_1 and A_2 are the first- and second-order Jahn–Teller coupling constants, respectively. Two parameters are required to describe the splitting of the electronic E state in a low-symmetry ligand-field

$$\hat{H}_{st} = e_\theta\hat{U}_\theta + e_\epsilon\hat{U}_\epsilon \tag{6}$$

where e_θ and e_ϵ are the tetragonal and orthorhombic components of the low-symmetry strain, respectively. The magnitude of these parameters defines a strain vector, $\vec{s}$, of magnitude, δ,

(46) Sugano, S.; Tanabe, Y.; Kamimura, H. *Multiplets of Transition Metal Ions In Crystals*; Academic Press: New York, 1970; p 305.

(47) Cohen-Tannoudji, C.; Diu, B.; Laloe, F. *Quantum Mechanics*; Wiley-Interscience: New York, 1977; Vol. 1, Chapter V, p 488.

Table 3. Summary of Single-Crystal X-Ray Diffraction Data, Collection Details, Structural Parameters, and Structural Refinements for $Rb_2Cr(H_2O)_6(SO_4)_2$ and $Cs_2Cr(H_2O)_6(SO_4)_2$

	$Rb_2Cr(H_2O)_6(SO_4)_2$ (100 K)	$Rb_2Cr(H_2O)_6(SO_4)_2$ (293 K)	$Cs_2Cr(H_2O)_6(SO_4)_2$ (100 K)	$Cs_2Cr(H_2O)_6(SO_4)_2$ (293 K)
crystal shape	block	block	block	block
crystal color	blue	blue	blue	blue
crystal size (mm³)	0.45 × 0.30 × 0.10	0.45 × 0.30 × 0.10	0.50 × 0.30 × 0.15	0.50 × 0.30 × 0.15
empirical formula	$H_{12}CrO_{14}Rb_2S_2$	$H_{12}CrO_{14}Rb_2S_2$	$H_{12}CrO_{14}Cs_2S_2$	$H_{12}CrO_{14}Cs_2S_2$
formula weight	523.16 g/mol	523.16 g/mol	618.04 g/mol	618.04 g/mol
crystal system	monoclinic	monoclinic	monoclinic	monoclinic
space group	$P2_1/c$	$P2_1/c$	$P2_1/c$	$P2_1/c$
unit cell	$a = 6.2163(12)$ Å	$a = 6.2446(9)$ Å	$a = 6.3181(11)$ Å	$a = 6.3352(9)$ Å
dimensions	$b = 12.3824(16)$ Å	$b = 12.4595(15)$ Å	$b = 12.8039(15)$ Å	$b = 12.8689(13)$ Å
	$c = 9.2600(15)$ Å	$c = 9.3270(14)$ Å	$c = 9.4930(16)$ Å	$c = 9.4987(13)$ Å
	$\alpha = 90°$	$\alpha = 90°$	$\alpha = 90°$	$\alpha = 90°$
	$\beta = 104.858(14)°$	$\beta = 105.269(12)°$	$\beta = 106.135(14)°$	$\beta = 106.283(11)°$
	$\gamma = 90°$	$\gamma = 90°$	$\gamma = 90°$	$\gamma = 90°$
volume	688.9(2) Å³	700.07(17) Å³	737.7(2) Å³	743.34(16) Å³
cell refinement params				
No. of reflns in cell refinement	3231	11757	22677	17200
angle range in cell refinement	$0.00° < \theta < 29.70°$	$0.00° < \theta < 29.55°$	$1.14° < \theta < 29.35°$	$1.14° < \theta < 29.55°$
Z	2	2	2	2
density (calculated)	2.522 g/cm³	2.482 g/cm³	2.782 g/cm³	2.761 g/cm³
radiation used	Mo Kα	Mo Kα	Mo Kα	Mo Kα
wavelength	0.71073 Å	0.71073 Å	0.71073 Å	0.71073 Å
linear absorption coefficient	8.217 mm⁻¹	8.087 mm⁻¹	5.983 mm⁻¹	5.937 mm⁻¹
temperature	100(2) K	293(2) K	100(2) K	293(2) K
diffractometer	STOE IPDS 2	STOE IPDS 2	STOE IPDS 2	STOE IPDS 2
scan method	rotation	rotation	rotation	rotation
absorption correction	empirical	empirical	empirical	empirical
max. and min. transmission	0.420 and 0.030	0.452 and 0.042	0.641 and 0.169	0.488 and 0.057
No. reflns measured	11917	11831	12995	14051
No. independent reflns	1937	1965	2032	2066
No. observed reflns	1815	1794	1790	1991
criterion for recognizing	$>2\sigma(I)$	$>2\sigma(I)$	$>2\sigma(I)$	$>2\sigma(I)$
R(int)	0.0967	0.0869	0.0592	0.0906
θ range for data collection	2.81–29.68°	2.79–29.66°	2.74–29.54°	2.74–29.55°
index ranges	$-8 \leq h \leq 8$	$-8 \leq h \leq 8$	$-8 \leq h \leq 8$	$-8 \leq h \leq 8$
	$-17 \leq k \leq 16$	$-17 \leq k \leq 16$	$-17 \leq k \leq 17$	$-17 \leq k \leq 17$
	$-12 \leq l \leq 12$	$-12 \leq l \leq 12$	$-13 \leq l \leq 13$	$-13 \leq l \leq 13$
$F(000)$	508	508	580	580
refinement method	full-matrix least-squares on F^2	full-matrix least-squares on F^2	full-matrix least-squares on F^2	full-matrix least-squares on F^2
final R indices [$I > 2\sigma(I)$]	$R_1 = 0.0339$ $wR_2 = 0.0824$	$R_1 = 0.0354$ $wR_2 = 0.0835$	$R_1 = 0.0313$ $wR_2 = 0.0634$	$R_1 = 0.0303$ $wR_2 = 0.0734$
R indices (all data)	$R_1 = 0.0365$ $wR_2 = 0.0842$	$R_1 = 0.0404$ $wR_2 = 0.0873$	$R_1 = 0.0397$ $wR_2 = 0.0683$	$R_1 = 0.0316$ $wR_2 = 0.0744$
H-locating and refining method	mixed	mixed	mixed	mixed
No. reflns used	1937	1965	2032	2066
No. refined params	88	88	88	88
goodness-of-fit on F^2	1.088	1.117	1.243	1.182
maximum e density	1.014 e Å⁻³	0.452 e Å⁻³	0.954 e Å⁻³	0.820 e Å⁻³
minimun e density	-1.249 e Å⁻³	-1.113 e Å⁻³	-0.853 e Å⁻³	-1.218 e Å⁻³

and angle, φ, in the e_θ, e_ϵ coordinate frame:

$$\delta = (e_\theta{}^2 + e_\epsilon{}^2)^{1/2}$$

$$\varphi = \tan^{-1}\left(\frac{e_\epsilon}{e_\theta}\right) + \alpha; \quad \text{if } e_\theta > 0, \alpha = 0°;$$

$$\text{if } e_\theta < 0, \alpha = 180° \quad (7)$$

The Hamiltonian was constructed as a matrix in a basis of products of the 10 electronic states and the states of the $\{Q_\theta,Q_\epsilon\}$ harmonic oscillator of dimension $N = \frac{1}{2}(n_v + 1)(n_v + 2)$, up to the level n_v. The matrix elements were evaluated and the lowest-lying eigenvalues and corresponding eigenvectors were found using a Lanczos diagonalization routine, as previously

described.[48] To ensure adequate convergence, n_v was set to 50, which required the diagonalization of a sparse matrix of the order $10 \times 1326 = 13\,260$.

The vibronic eigenfunctions of the Hamiltonian, Ψ, are expressed as linear combinations of the basis functions

$$\Psi = \sum_i \sum_j \sum_{k+l=0}^{n_v} a_{ijkl}|\psi_i,M_{s\,j},n_{\theta k},n_{\epsilon\,l}\rangle \quad (8)$$

where ψ_i spans the two-orbital components of the ^5E_g ground term, M_s specifies the electron spin, and n_θ and n_ϵ are the quantum numbers of the harmonic oscillators.

(48) Tregenna-Piggott, P. L. W. *Adv. Quantum Chem.* **2003**, *44*, 461.

An analytical expression for the E⊗e Jahn−Teller potential energy surface is obtained by diagonalization of the 2 × 2 Hamiltonian matrixes, omitting the terms in the kinetic energy and plotting the energy as a function of Q_θ and Q_ϵ. Contour plots were rendered using Mathematica 5.

3.2. Calculation of the Experimental Quantities. 3.2.1. Bond Lengths. The mean nuclear displacements at a given temperature were calculated by first evaluating the expectation values of $\hat{q}_\theta$ and $\hat{q}_\epsilon$ in each of the thermally populated vibronic states and similarly for $\langle \hat{q}_\epsilon \rangle$.

$$\langle \hat{q}_\theta \rangle = \sqrt{\frac{\hbar}{\mu\omega}} \langle \Psi | \hat{Q}_\theta | \Psi \rangle =$$

$$\sqrt{\frac{\hbar}{\mu\omega}} \sum_{i,i',j,j'} \sum_{l+m=0}^{n_v} \sum_{l'+m'=0}^{n_v'} a_{ijlm}^* a'_{i'j'l'm'} \langle n_{\theta l} | \hat{Q}_\theta | n'_{\theta'l'} \rangle \delta_{ii'} \delta_{jj'} \delta_{mm'} =$$

$$\sqrt{\frac{\hbar}{\mu\omega}} \sum_{i,i',j,j'} \sum_{l+m=0}^{n_v} \sum_{l'+m'=0}^{n_v'} \left(a_{ij(l+1)m}^* a'_{i'j'l'm'} \sqrt{\frac{l'+1}{2}} + \right.$$

$$\left. a_{ij(l-1)m}^* a'_{i'j'l'm'} \sqrt{\frac{l'}{2}} \right) \delta_{ii'} \delta_{jj'} \delta_{mm'} \quad (9)$$

The distortion of the molecule along the components of the ν_2-(MO_6) vibration may be described as displacements of the oxygen atoms along each of the six Cr−O$_i$ bond vectors or, more succinctly, in terms of the magnitude of the displacement vector, ρ, and the angle, ϕ, which it makes to the $\hat{Q}_\theta$ displacement vector in the two-dimensional $\hat{Q}_\theta$, $\hat{Q}_\epsilon$ coordinate space:

$$\Delta r_1 = \Delta r_4 = \frac{\rho}{\sqrt{12}}(2\cos\phi) = \frac{1}{\sqrt{12}}(2\langle \hat{q}_\theta \rangle),$$

$$\Delta r_2 = \Delta r_5 = \frac{\rho}{\sqrt{12}}(-\cos\phi + \sqrt{3}\sin\phi) =$$

$$\frac{1}{\sqrt{12}}(-\langle \hat{q}_\theta \rangle + \sqrt{3}\langle \hat{q}_\epsilon \rangle),$$

$$\Delta r_3 = \Delta r_6 = \frac{\rho}{\sqrt{12}}(-\cos\phi - \sqrt{3}\sin\phi) =$$

$$\frac{1}{\sqrt{12}}(-\langle \hat{q}_\theta \rangle - \sqrt{3}\langle \hat{q}_\epsilon \rangle) \quad (10)$$

Finally, the nuclear displacements at a given temperature were calculated as the Boltzmann average of the geometric properties of the individual vibronic energy levels.

3.2.2. EPR Spectrum. High-temperature EPR data on copper(II) salts are commonly interpreted under the assumption that the time scale of the experiment is slow compared to relaxation between states with different electronic and nuclear coordinates.[16] The resonance field is calculated, quite simply, from the Boltzmann-weighted g value over the thermally populated states. In this section, a generalized Silver and Getz model[49] for the dynamic Jahn−Teller effect is developed for spin systems with $S > 1/2$.

(49) Silver, B. L.; Getz, D. *J. Chem. Phys.* **1978**, *61*, 638.

The effective ${}^5E_g$ (O_h) Hamiltonian may be written as:

$$\hat{H}_{cub} = \frac{-b}{2}(\hat{U}_\theta \hat{S}_\theta + \hat{U}_\epsilon \hat{S}_\epsilon) \quad (11)$$

where

$$\hat{S}_\theta = \hat{S}_z^2 - \frac{1}{3}S(S+1); \quad S_\epsilon = \frac{1}{\sqrt{3}}(\hat{S}_x^2 - \hat{S}_y^2) \quad (12)$$

The value of b in this system is of the order of 4 cm^{-1},[9] which is much smaller than the other terms in the vibronic Hamiltonian. $\hat{H}_{cub}$ can be treated as a perturbation whenever the vibronic levels are strongly localized in a given potential minimum. Diagonalizing the vibronic Hamiltonian in a basis spanning ψ_i, n_θ, and n_ϵ and evaluating the expectation value of $\hat{H}_{cub}$ over the ith set of five states, we obtain:

$$\langle \Psi(\psi, n_\theta, n_\epsilon) | \hat{H}_{cub} | \Psi(\psi, n_\theta, n_\epsilon) \rangle_i =$$

$$\frac{-b}{2}(\langle \Psi(\psi, n_\theta, n_\epsilon) | \hat{S}_\theta \hat{U}_\theta | \Psi(\psi, n_\theta, n_\epsilon) \rangle_i +$$

$$\langle \Psi(\psi, n_\theta, n_\epsilon) | \hat{S}_\epsilon \hat{U}_\epsilon | \Psi(\psi, n_\theta, n_\epsilon) \rangle_i) =$$

$$\frac{-b}{2}\hat{S}_\theta \langle \hat{U}_\theta \rangle_i + \frac{-b}{2}\hat{S}_\epsilon \langle \hat{U}_\epsilon \rangle_i \quad (13)$$

The magnetic response may be conveniently described by the conventional spin-Hamiltonian:

$$\hat{H}_s = \beta B_x g_{xx} \hat{S}_x + \beta B_y g_{yy} \hat{S}_y + \beta B_z g_{zz} \hat{S}_z +$$

$$D\left[\hat{S}_z^2 - \frac{1}{3}S(S+1)\right] + E[\hat{S}_x^2 - \hat{S}_y^2] \quad (14)$$

Comparison of eqs 13 and 14 leads to the following expressions for the parameters D and E:

$$D_i = \frac{-b}{2}\langle \hat{U}_\theta \rangle_i, \quad E_i = \frac{-b}{2\sqrt{3}}\langle \hat{U}_\epsilon \rangle_i \quad (15)$$

The way in which these zfs parameters are averaged can be illustrated by considering a case where only three vibronic states are populated. Using values for $\hbar\omega$, A_1, A_2, and A_3 of 254, −900, 33, and 0 cm^{-1}, respectively, and levels of strain that localize the states in a given potential minima without perturbing the warped Mexican-hat potential energy surface significantly, the three lowest lying states have values of $(1,0)$, $(-(1/2), \sqrt{3}/2)$, and $(-(1/2), -(\sqrt{3}/2))$ for $(\langle U_\theta \rangle_i, \langle U_\epsilon \rangle_i)$. These, in turn, correspond to the three Jahn−Teller configurations with elongation of the z, x, and y bond lengths. The D and E values for these three states will therefore be given by $(-(b/2), 0)$, $(-(b/4), (b/4))$, and $(-(b/4), -(b/4))$, corresponding to an axial zero-field-splitting of equal magnitude but with the principal axis along the z, x, and y axes, respectively.

The relative energies, Δ_i, and Boltzmann populations, P_i, of these three states can be approximated by

$$\Delta_i = e_\theta \langle \hat{U}_\theta \rangle_i + e_\epsilon \langle \hat{U}_\epsilon \rangle_i$$

$$P_i = \frac{e^{-\Delta_i/kT}}{\sum_j e^{-\Delta_j/kT}} \quad (16)$$

In the fast-hopping regime, the averaged D and E values are given by the Boltzmann-weighted average of the individual D and E values for each vibronic state:

$$D_{av} = -P_1\frac{b}{2} + (P_2 + P_3)\frac{b}{4}$$

$$E_{av} = (P_3 - P_2)\frac{b}{4} \tag{17}$$

At low temperatures, only the lowest well is populated, and average D and E values are simply those of that configuration. As the temperature increases and the second well is populated, the D value is seen to decrease and the E value increases. Eventually in the high-temperature limit, when $P_1 \approx P_2 \approx P_3$, both D and E approach 0. By contrast, if the time scale of the EPR experiment is much faster than the hopping rate, then the resultant spectra will be a superposition of the spectra from each configuration. The powder spectrum for each of the three configurations is identical in this case, and therefore, there will be no change with temperature.

3.2.3. INS Spectrum. The interaction time in an inelastic neutron scattering experiment may be estimated from the time it takes for a neutron to traverse the breadth of the paramagnetic scattering species, from which a value of the order of 10^{-12} s is obtained,[50] which is very short compared to the EPR time scale. Assuming that interstate relaxation does not occur in the course of a scattering event, the INS spectrum can be calculated very simply as the Boltzmann-weighted superposition of all possible transitions between the eigenfunctions of the vibronic Hamiltonian, occurring in the energy range of interest. In the instance where intermolecular magnetic interactions are weak, the differential neutron cross-section, I_{INS}, between states with eigenvalues E_{ini} and E_{fin} and eigenvectors Ψ_{ini} and Ψ_{fin}, is proportional to,[2]

$$I_{INS} \propto \exp\left(\frac{-E_i}{kT}\right)F^2(Q)\cdot|\langle\Psi_{fin}|\mu_\perp|\Psi_{ini}\rangle|^2 \tag{18}$$

where $\mu_\perp$ is the component of the magnetic moment operator perpendicular to the scattering vector, Q, and $F(Q)$ is the magnetic form factor. The calculation of the matrix element $\langle\Psi_{fin}|\hat{\mu}_\perp|\Psi_{ini}\rangle$ proceeds according to:

$$\langle\Psi_{fin}|\hat{\mu}_\perp|\Psi_{ini}\rangle =$$
$$\sum_{i,i',j,j'}\sum_{l+m=0}^{n_v}\sum_{l'+m'=0}^{n'_v} a_{ijlm}{}^* a'_{i'j'l'm'}\langle\psi_i,M_{sj}|\hat{\mu}_\perp|\psi_{i'},M_{sj'}\rangle\delta_{ll'}\delta_{mm'} \tag{19}$$

where a and a' denote the coefficients defining Ψ_{fin} and Ψ_{ini}, respectively. For the present system, the states are connected by the spin component of the magnetic moment operator only, in which case,[2,9]

$$|\langle\Psi_f|\mu_\perp|\Psi_i\rangle|^2 =$$
$$|\langle\Psi_f|\hat{s}_\perp|\Psi_i\rangle|^2 =$$
$$\frac{1}{3}(2|\langle\Psi_f|\hat{s}_z|\Psi_i\rangle|^2 + |\langle\Psi_f|\hat{s}_+|\Psi_i\rangle|^2 + |\langle\Psi_f|\hat{s}_-|\Psi_i\rangle|^2) \tag{20}$$

All intensities were calculated assuming $Q = 0$ Å^{-1}, where $F(Q)$ is equal to unity. The calculated INS transitions were folded with a Gaussian band shape, with constant width across the spectrum.

In the regime where intramolecular reorientations of the Jahn−Teller complex are respectively slow and fast on the EPR and INS time scales, the procedure for calculating the effective spin-Hamiltonian parameters depends on the techniques by which the information was obtained. For an EPR experiment, one must average the D and E values with respect to a given coordinate frame, as described in section 3.2.2. Effective spin-Hamiltonian parameters are extracted from an INS experiment by fitting the spectrum to a series of Gaussian functions and then by modeling the energies at which the Gaussians are centered with the eigenvalues of an $S = 2$ spin Hamiltonian. Theoretical values of D and E may be obtained in exactly the same way, but the magnitudes of the parameters will not be independent of the width assigned to each transition. Alternatively, this lengthy procedure may be approximated by calculating D and E in each of the thermally populated manifolds, ensuring that $0 < E/D < \frac{1}{3}$, and then calculating the Boltzmann-weighted average of these parameters.

4. Results

4.1. Inelastic Neutron Scattering. INS spectra of (ND₄)₂-Cr(D₂O)₆(SO₄)₂ were collected between 1.5 and 297 K at regular temperature intervals. At 1.5 K, bands at 7.107(9) and 7.63(1) cm^{-1} are observed (labeled I and II in Figure 1). At 10 K, further transitions, labeled β and γ, grow in at 2.20(2) and 2.27(2) cm^{-1}, respectively, commensurate with the proposed energy level diagram in Figure 2. The transition α could not be resolved with the instrumental settings used, being subsumed into the elastic band. The relative intensities and energies of the INS transitions are found to vary considerably, as the temperature is increased from 100 to 297 K, with a concomitant increase in bandwidths.

INS spectra were also obtained for Rb₂Cr(D₂O)₆(SO₄)₂ and are presented in Figure 3. At 10 K, transitions are observed at 2.01(2), 2.86(2), 6.835(2), and 7.661(3) cm^{-1} in an energy pattern similar to that of the ammonium salt. The change in energies of these INS transitions upon increasing temperature to 250 K is significant but not as marked as that found for the ammonium salt.

The intensities of transitions I, II, β, and γ were found to decrease with increasing momentum transfer, Q, indicating that they correspond to transitions of magnetic origin.[51] In Figure 4, plots of the normalized sum of the intensities of transitions I and II (at 10 K) are presented as a function of Q, for both the Rb and ND₄ salts. The experimental points are represented by symbols, while the line depicts the expected intensities calculated using the tabulated coefficients for the spin-only magnetic

---

(50) From the de Broglie relation, a neutron with a wavelength of 5.4 Å has a speed of 732 m s^{-1}. The [Cr(OD₂)₆]$^{2+}$ cation has as an approximate diameter of 5.5 Å. Therefore, the time it takes for the neutron to traverse the breadth of the scattering species is $5.5 \times 10^{-10}/732 = 7.5 \times 10^{-13}$ s.

(51) Squires, G. L. *Thermal Neutron Scattering*; Cambridge University Press: New York, 1978.
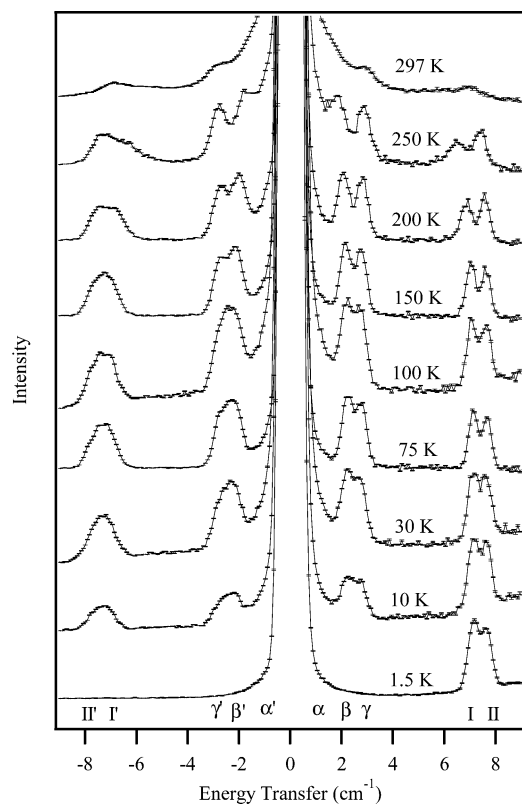
Figure 1. INS spectra of $(ND_4)_2Cr(D_2O)_6(SO_4)_2$, measured on FOCUS, between 1.5 and 297 K with an incident neutron wavelength of 5.3 Å. The labeling scheme follows that of the energy level diagram depicted in Figure 2. Error bars are shown at the 1 esd level.
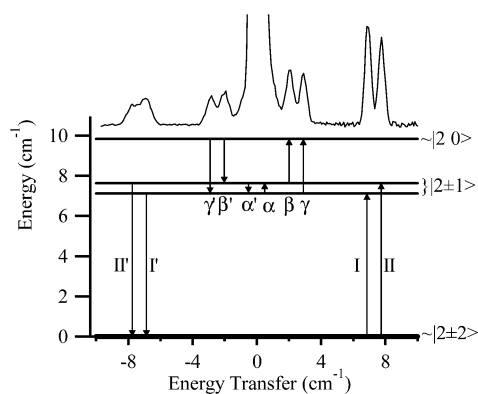

Figure 2. Energy level diagram for an $S = 2$ system, corresponding to the observed transitions in $(ND_4)_2Cr(D_2O)_6(SO_4)_2$. The INS transitions for neutron energy gain (left) and loss (right) are indicated by arrows.

form factor of Cr(II).[52] The experimental Q was calculated from the average binned detector angle, θ, and the incident neutron wavelength, λ, as

$$Q = \frac{4\pi \sin(\theta)}{\lambda} \qquad (21)$$

The INS bands are assigned to transitions within the ^5A_g (C_i) ground term, which is split into second order by spin−orbit coupling. The zero-field-splitting is conveniently described by the effective spin Hamiltonian, acting in a basis of the five $S = 2$ spin functions given in eq 14, with $B = 0$. Least-squares fitting

(52) Brown, P. J. *International Tables for Crystallography C*; Kluwer Academic Publishers: Dordrecht, The Netherlands; Chapter 4.4.5, p 391.
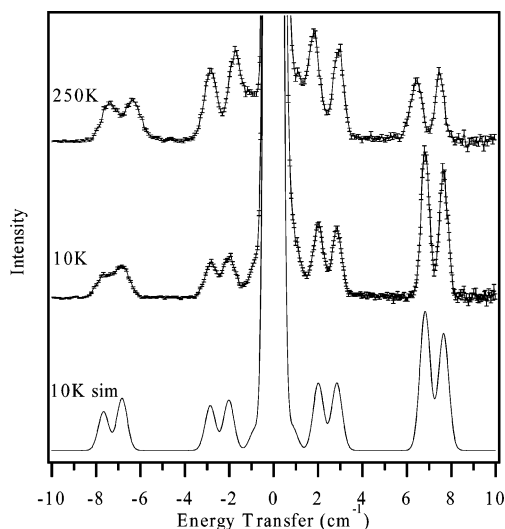
Figure 3. INS spectra of $Rb_2Cr(D_2O)_6(SO_4)_2$, measured on FOCUS, at 10 and 250 K with an incident neutron wavelength of 5.4 Å. The 10 K simulation was calculated from eqs 14, 18, and 20, with $D = -2.411$ cm^{-1} and $E = 0.139$ cm^{-1}, obtained from a least-squares fit of the observed transition energies to the eigenvalues of the spin Hamiltonian. Error bars are shown at the 1 esd level.
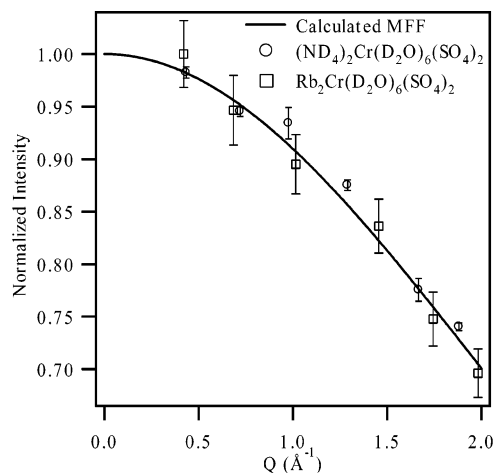

Figure 4. Plots of the summed INS intensities of transitions I and II at 10 K for $(ND_4)_2Cr(D_2O)_6(SO_4)_2$ and $Rb_2Cr(D_2O)_6(SO_4)_2$ as a function of momentum transfer, Q. The solid line indicates the theoretical spin-only magnetic form factor for Cr(II).

of the eigenvalues of eq 14 to the experimentally observed excitation energies at 10 K, yielded $D = -2.454(3)$ cm^{-1} and $E = 0.087(3)$ cm^{-1} for the ammonium salt, and $D = -2.411(1)$ cm^{-1} and $E = 0.139(1)$ cm^{-1} for the rubidium salt. It is evident, simply from comparison of the spectra, that the value of E is somewhat larger for the rubidium salt. The experimental and calculated energies and intensities are presented in Table 4. The simulated spectrum in Figure 3 was calculated using the eigenvalues and eigenfunctions of eq 14, with the zfs parameters extracted from the 10 K spectrum, and agrees very well with the experimental spectrum.

Values for D and E were similarly extracted at each temperature. For the ammonium salt, a pronounced temperature dependence in these parameters was established. As shown in Figure 5, the magnitude of D decreases and the magnitude of E increases upon increasing temperature, particularly in the 100−297 K range, reaching $D = 2.29(2)$ cm^{-1} and $E = 0.16$-(3) cm^{-1} at 250 K. For the rubidium salt, the change is more
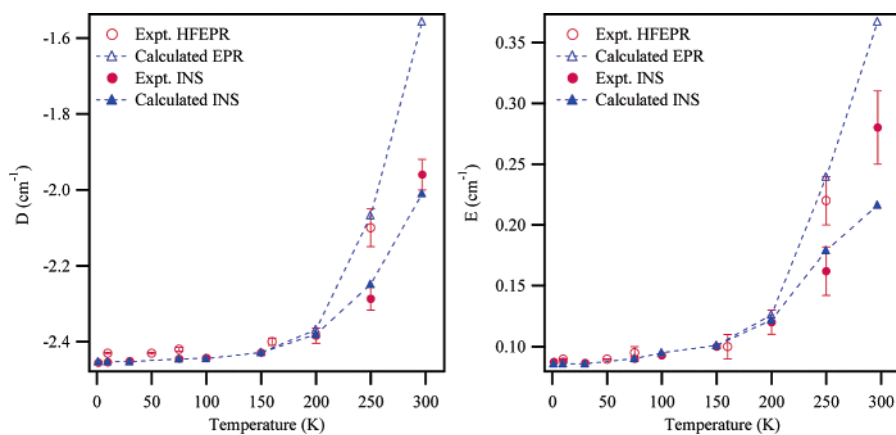
Figure 5. Experimental and calculated values of the parameters D and E for $(ND_4)_2Cr(D_2O)_6(SO_4)_2$ as a function of temperature. Estimated errors are indicated at the 1 esd level. The calculated values of D and E used the following parameter set: $\hbar\omega = 254$, $B = 637$, $C = 2640$, $\zeta = 193.2$, $A_1 = -900$, $A_2 = 33$, $A_3 = 0$, $e_\theta = 700$ cm^{-1}, while values of Δ_O and e_ϵ were varied according to Table 5. The points labeled "calculated EPR" were generated by averaging the D and E values with respect to a given coordinate frame, whereas the points labeled "calculated INS" were generated by averaging the absolute magnitudes after a transformation such that $0 < E/D < \frac{1}{3}$, as described in sections 3.2.2. and 3.2.3. Note that the dashed line is a guide for the eye only.

Table 4. Experimental and Calculated INS Transition Energies and Intensities for $(ND_4)_2Cr(D_2O)_6(SO_4)_2$ and $Rb_2Cr(D_2O)_6(SO_4)_2$ at 10 K (Intensities Were Scaled to Transition I)

	$(ND_4)_2Cr(D_2O)_6(SO_4)_2$ 10 K $D = -2.454(3)$ cm^{-1} $E = 0.087(3)$ cm^{-1}				$Rb_2Cr(D_2O)_6(SO_4)_2$ 10 K $D = -2.411(1)$ cm^{-1} $E = 0.139(1)$ cm^{-1}			
	obs. energy	calcd energy	obs. intensity	calcd intensity	obs. energy	calcd energy	obs. intensity	calcd intensity
β	2.20 (2)	2.201	0.44(2)	0.49	2.01(2)	2.02	0.56(3)	0.48
γ	2.72 (2)	2.726	0.44(3)	0.49	2.86(2)	2.85	0.53(3)	0.49
I	7.107(9)	7.109	1.00(5)	1.00	6.835(2)	6.841	1.00(1)	1.00
II	7.63 (1)	7.634	0.89(5)	0.90	7.661(3)	7.676	0.88(1)	0.84
β'	−2.20 (2)	−2.201		0.36	−2.02(2)	−2.02	0.33(1)	0.36
γ'	−2.72 (2)	−2.726		0.33	−2.83(2)	−2.85	0.30(1)	0.32
I′	−7.107(9)	−7.109		0.36	−6.83(2)	−6.841	0.37(1)	0.38
II′	−7.63 (1)	−7.634		0.30	−7.66(2)	−7.676	0.25(1)	0.28

modest; at 250 K, the value of D is reduced to $-2.292(3)$ cm^{-1} and E increases to $0.178(1)$ cm^{-1}.

4.2. EPR. Preliminary HFEPR experiments demonstrated the need for extremely well ground samples. With great care in grinding and in immobilizing the powder using a low melting point wax, the quality of the powder EPR spectra was improved substantially. Signals attributable to chromium(III) species were observed in all of the spectra collected, with chromium(II) compounds being extremely susceptible to oxidation. Spectra were recorded sweeping upfield and then downfield, typically using a scan rate of 8 mT/s, affording the collection of high-quality spectra in a reasonable time period. No nuclear hyperfine structure was observed; this is not surprising in view of the low natural abundance (9.5%) of the ^{53}Cr isotope and the large EPR bandwidths resulting from dipole−dipole interactions between neighboring Cr(II) centers.

Both hydrogenous and deuterated $(NH_4)_2Cr(H_2O)_6(SO_4)_2$ EPR samples were examined, but no dependence of the resonance positions on the isotope was found. The resonance positions varied markedly on when cooled to ∼150 K, below which little change was observed. Analysis of the spectra at 5 and 25 K yielded the following parameters: $D = -2.43(1)$ cm^{-1}, $E = 0.0895(5)$ cm^{-1}, $g_{xx} = g_{yy} = 1.990(5)$, and $g_{zz} = 1.955(5)$. Representative HFEPR spectra recorded at ∼95 and ∼285 GHz, shown in Figure 6, are reproduced extremely well by simulations using these parameters. The zero-field-splitting parameters were determined as a function of temperature, up to 250 K, and are displayed in Figure 5, along with the values determined by INS.

In the 5−150 K temperature range, the EPR spectra could be simulated satisfactorily with values of D and E consistent with those determined by INS. However, at 250 K, modeling of the EPR and INS data sets required a different set of zero-field-splitting parameters, as shown in Figure 5. The resonant field positions and line widths of spectra recorded at X- and Q-band were strongly temperature dependent in the 120−250 K temperature range. Above ∼225 K, the transitions attributable to Cr^{2+} broaden rapidly and lose intensity, becoming unobservable at room temperature. This explains why previous attempts to record the X-band spectra were unsuccessful.[24] The spectra were simulated with the g values fixed at the values derived from the low-temperature HFEPR data. Due to the broad line widths and relatively featureless spectra, the D and E parameters could not be determined accurately. However, the variation with temperature is clear and consistent with that of the HFEPR data. The spectra are included as Supporting Information. We conclude that for the $(NH_4)_2Cr(H_2O)_6(SO_4)_2$ salt, there is a definite difference between the zero-field-splitting parameters derived from the 250 K INS and EPR spectra.

EPR spectra have been previously recorded for $Rb_2Cu(H_2O)_6(SO_4)_2$ at 4.2 and 300 K, and a minimal variation in the observed g values has been reported.[53] By contrast, EPR studies on the chromium(II) salt reveal a significant temperature dependence in the ground-state spin-Hamiltonian parameters. Analysis of HFEPR spectra for $Rb_2Cr(H_2O)_6(SO_4)_2$ yielded $D = -2.41(1)$

(53) Petrashen, V. E.; Yablokov, Y. V.; Davidovich, R. L. *Phys. Status Solidi B* **1980**, *101*, 117.

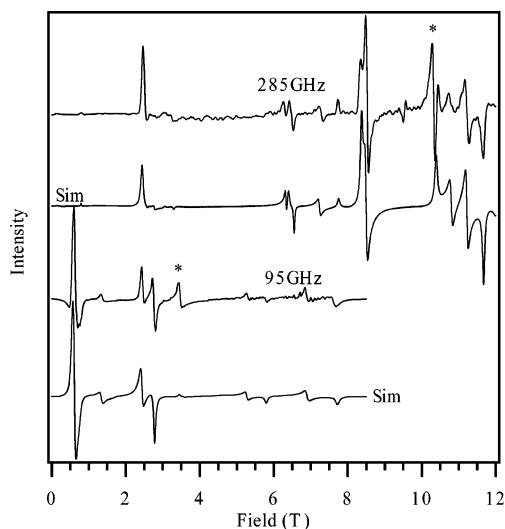**Figure 6.** Experimental HFEPR spectra of $(ND_4)_2Cr(D_2O)_6(SO_4)_2$, obtained using excitation frequencies of 284.9973 (25 K) and 94.9991 GHz (5 K) and simulations using the parameters $D = -2.43$ cm^{-1}, $E = 0.0895$ cm^{-1}, $g_{xx} = g_{yy} = 1.990$, $g_{zz} = 1.955$, and a line width of 0.05 T. Resonances attributable to Cr^{3+} are indicated with an asterisk (*).

cm^{-1}, $E = 0.135(5)$ cm^{-1}, $g_{xx} = g_{yy} = 1.995(5)$, and $g_{zz} = 1.96(2)$ at 10 K and $D = -2.30(3)$ cm^{-1}, $E = 0.185(5)$ cm^{-1}, $g_{xx} = g_{yy} = 1.995(5)$, and $g_{zz} = 1.96(2)$ at 250 K. For this salt, the zfs parameters are in accordance with the analysis of the INS data. Variable-temperature X- and Q-band EPR spectra, presented in Supporting Information, show a pronounced change in the resonance field positions above 200 K. X-band spectra were also recorded for the $Cs_2Cr(H_2O)_6(SO_4)_2$ salt and are presented in Supporting Information. As no HFEPR data for this compound were collected, the spectra were simulated with the g values determined for the rubidium salt. At 7 K, D and E were estimated as $-2.31(4)$ and $0.083(2)$ cm^{-1}, respectively. The X-band spectra exhibited a temperature dependence similar to that observed for the rubidium salt.

4.3. Structural Data. Variable-temperature single-crystal and powder diffraction measurements on the $(NH_4)_2Cr(H_2O)_6(SO_4)_2$ Tutton's salt afford precise structural determinations, at regular temperature intervals, in the 10−300 K temperature range. Upon increasing temperature, the unit-cell parameters, a, b, and β, of the chromium salt decrease, and the c parameter increases. The determined Cr−O bond lengths are in agreement with values previously reported at 4.2,[11,12] 84,[13] and 295 K.[14] When the labeling scheme given in ref 54 is adopted, the Cr−O(7) and Cr−O(8) bond lengths start to converge above ~150 K, while the Cr−O(9) bond length decreases marginally, as shown in Figure 7. The onset of this behavior, attributable to the dynamical nature of the Jahn−Teller effect, is discerned at lower temperatures in the copper analogue. Fractional coordinates and anisotropic thermal parameters for each structure are given in Supporting Information.

The single-crystal X-ray diffraction measurements on the rubidium and cesium chromium salts reveal structures consistent with those of their copper counterparts.[55] For both chromium salts, marginal differences are observed between the atomic
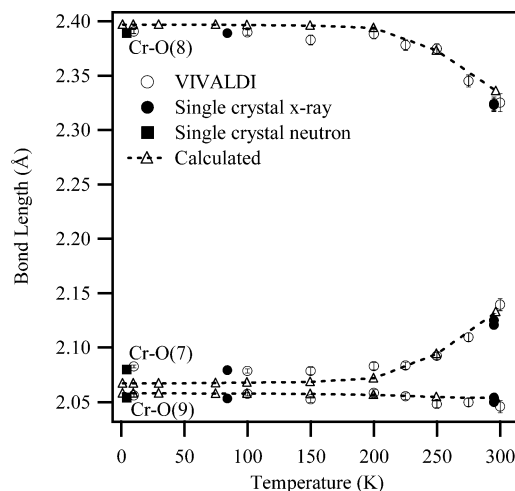
(54) Dobe, C.; Carver, G.; Tregenna-Piggott, P. L. W.; McIntyre, G. J.; Augustyniak-Jablokow, M. A.; Riley, M. J. *Inorg. Chem.* **2003**, *42*, 8524.
(55) Whitnall, J. M.; Kennard, C. H. L. *J. Solid State Chem.* **1977**, *22*, 379−383.

Figure 7. Temperature dependence of the Cr−O bond lengths in $(NX_4)_2$-$Cr(X_2O)_6(SO_4)_2$. Single-crystal Laue neutron data were collected on VIVALDI between 10 and 300 K (X = H). X-ray data were taken from refs 11 (X = H, 295 K), 13 (X = H, 84 and 295 K), and monochromatic single-crystal neutron data from ref 14 (X = D, 4.2 K). The open triangles denote theoretical values calculated using the parameters given in Table 5, while the dashed line serves only as a guide for the eye. Error bars are shown at 1 esd.
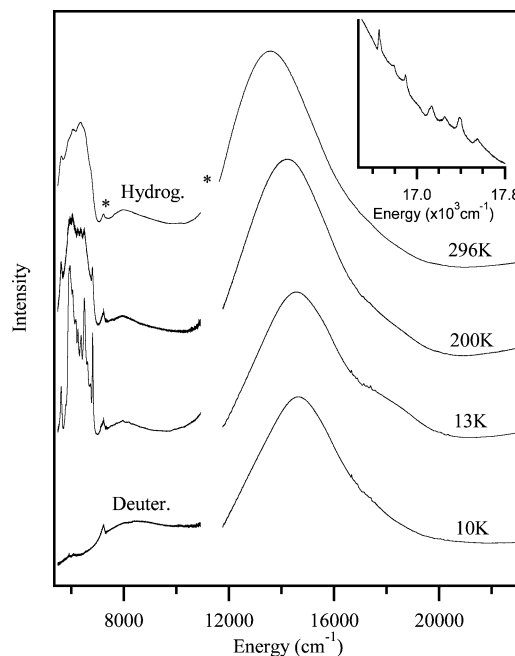

Figure 8. Optical absorption spectra of single-crystal $(ND_4)_2Cr(D_2O)_6$-$(SO_4)_2$ in both the hydrogenous and deuterated forms as a function of temperature. Spectral bandwidth is 0.25 nm. The artifacts indicated by asterisks are due to detector changeovers. The inset shows an expanded view of the 10 K hydrogenous data in the spectral region of the observed spin-flip transitions.

positions determined at 100 K and those determined at room temperature. The Cr−O bond lengths are tabulated in Supporting Information.

4.4. Optical Spectra. Unpolarized single-crystal absorption spectra of hydrogenous and deuterated samples of $(NH_4)_2Cr$-$(H_2O)_6(SO_4)_2$ were collected in the 13−296 K temperature range. Selected spectra are presented in Figure 8. At 13 K, the spectrum consists of broad features centered at ~8000, ~14 550, and ~18 050 cm^{-1}, with weaker, sharper features between 16 660 and 19 830 cm^{-1}. The spectrum of the deuterated sample is analogous, save for the absence of prominent features centered

at ~5000 cm^{-1}, attributable to overtones of O−H stretching vibrations and the reduced shoulder at ~18 050 cm^{-1}.

The spectrum is consistent with that expected for an octahedrally coordinated high-spin d^4 complex, subject to a tetragonal distortion.[56] The band at ~8000 cm^{-1} is assigned as the transition between the tetragonally split components of the ^5E_g (O_h) ground term. When low-symmetry strain and higher-order contributions are neglected, the splitting of the ^5E_g ground term, $\Delta(^5E_g)$, is given by

$$\Delta(^5E_g) = 4E_{JT} = 4\left(\frac{A_1^{\,2}}{2\hbar\omega}\right) \qquad (22)$$

The band occurs at a position similar to that found for the corresponding $\Delta(^2E_g)$ transition in the copper Tutton's salts, suggesting similar values for the linear Jahn−Teller coupling constants. The energy of the NIR band is not observed varying with temperature.

The prominent band at ~14 550 cm^{-1} and the shoulder at ~18 050 cm^{-1} are assigned to transitions from the ^5A_g (C_i) ground state to components of the $^5T_{2g}$ (O_h) ground term, split by the tetragonal field and excited-state Jahn−Teller effects. Assuming the barycenter of the $^5T_{2g}$ (O_h) term lies midway between these bands, a value for the octahedral splitting parameter, Δ_O, of [(14 550 + 18 050)/2 − 8000/2] = 12 300 cm^{-1} is obtained. The data suggest that this parameter diminishes with increasing temperature as the crystal lattice expands, with the prominent band falling to 13 640 cm^{-1} at 296 K. This interpretation is tentative, however, as the position of the higher-energy shoulder cannot be determined precisely above ~200 K.

The sharp bands observed at ~17 000 and ~20 000 cm^{-1} broadened with increasing temperature and were no longer observable at room temperature, consistent with their assignment to spin-flip transitions. To facilitate the interpretation of the spectrum, calculations were undertaken using the LIGFIELD[57] program, employing all states arising from the d^4 electronic configuration and parametrizing the ligand-field using the Angular Overlap Model (AOM). An unambiguous assignment of this spectral region proved impossible. Setting the Racah parameters, B and C, to 80% of their free-ion values ($B = 637$, $C = 2640$),[58] triplet states were calculated at energies consistent with the sharp transitions seen at ~17 000 and ~20 000 cm^{-1}, whose energies were only weakly dependent upon Δ_O. It may be stated, therefore, that with these reasonable choices of B and C, the calculated energy level diagram is consistent with the experimental spectrum. A similar approach was adopted to interpret the optical spectrum of Cr(H$_2$O)$_4$Cl$_2$.[22]

5. Discussion

The INS, EPR, UV−vis, and crystallographic data of the chromium(II) Tutton's salts, presented in this work, constitute the most thorough characterization to date of an octahedrally coordinated high-spin d^4 complex. All of the experimental quantities from 5 to 298 K must be accounted for within a self-consistent framework, in which the vibrational coordinates of
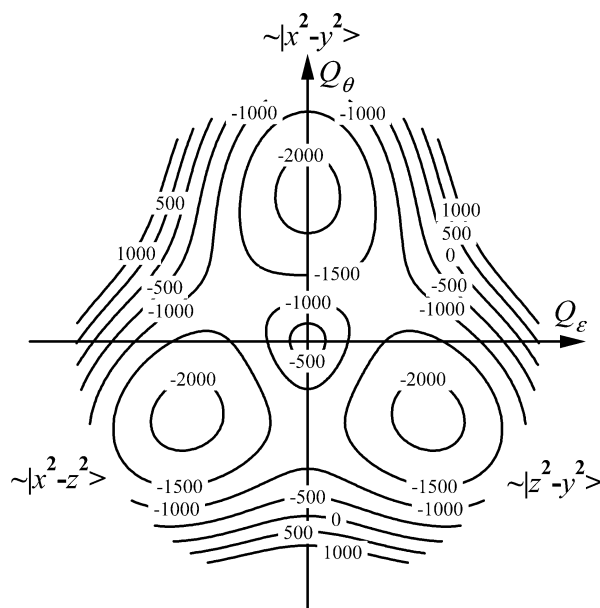

Figure 9. Contour plot of the E⊗e Jahn−Teller potential energy surface, calculated with the following parameters: $A_1 = -900$ cm^{-1}, $A_2 = 33$ cm^{-1}, $A_3 = 0$, $\hbar\omega = 254$ cm^{-1}.

the complex are considered explicitly. To this end, the electronic and molecular structures are calculated from the eigenvalues and eigenvectors of $^5E⊗e$ vibronic Hamiltonian, as described in Theory section.

Comparison of the optical spectra of copper(II) and chromium(II) Tutton's salts suggests similar magnitudes for the E⊗e Jahn−Teller coupling interaction in the two hexa-aqua cations. Hence, the electronic and molecular properties of the [Cr(D$_2$O)$_6$]$^{2+}$ cation were calculated with A_1, A_2, and A_3 set to -900, 33, and 0 cm^{-1}, respectively, which are the values used to interpret the majority of data obtained for the ammonium copper(II) Tutton's salts.[16] The phonon energy, $\hbar\omega$, was set to 254 cm^{-1}, based upon single-crystal Raman measurements.[59] A contour plot of the warped Mexican-hat potential energy surface, calculated with these parameters, is shown in Figure 9. On the periphery of the plot is shown the form of the orbital component of the wave function for $\phi = 0$, 120, and 240°. For a vibronic state localized at $\phi = 240°$, the expectation values of the nuclear coordinates equate to a tetragonally elongated octahedron of exact D_{4h} symmetry. The orbital component of the electronic function is of the form, $\sim|x^2 - z^2\rangle$, and the ground state $S = 2$ manifold may be described by an axially symmetric spin Hamiltonian.

The fact that a distortion of the CrO$_6$ framework is observed is a consequence of anisotropic strain, which lifts the degeneracy of the three potential wells. At low temperatures, the complex is frozen in the configuration of minimum energy; as the temperature is raised and higher-lying vibronic states are populated, the [Cr(H$_2$O)$_6$]$^{2+}$ cation can fluctuate between different structural conformations. Crystallography is a measure of the space-averaged structure and is a sensitive probe of the adiabatic potential energy surface. We begin, therefore, with an analysis of the variation of the observed bond lengths with

(56) Tregenna-Piggott, P. L. W.; Weihe, H.; Barra, A.-L. *Inorg. Chem.* **2003**, *42*, 8504.

(57) Bendix, J. *LIGFIELD*, version 0.92; Department of Chemistry, H. C. Orsted Institute, University of Copenhagen: Copenhagen, Denmark.

(58) Bendix, J.; Brorson, M.; Schaeffer, C. E. *Inorg Chem.* **1993**, *32*, 2838−2849.

(59) Carver, G.; Dobe, C.; Tregenna-Piggott, P. L. W. Unpublished work. (b) Rajagopal, P.; Aruldhas, G. *J. Solid State Chem.* **1989**, *80*, 303−307. (c) Barashkov, M. V.; Zazhogin, A. A.; Komyak, A. I.; Shashkov, S. N. *J. Appl. Spectrosc.* **2000**, *67*, 605−611.

Table 5. Values of Δ_O and e_ϵ Used to Reproduce the Experimental Data for $(ND_4)_2Cr(D_2O)_6(SO_4)_2$ and $Rb_2Cr(D_2O)_6(SO_4)_2$[a]

	(ND$_4$)$_2$Cr(D$_2$O)$_6$(SO$_4$)$_2$				Rb$_2$Cr(H$_2$O)$_6$(SO$_4$)$_2$			
T (K)	Δ_O (cm^{-1})	e_ϵ (cm^{-1})	$\langle\rho\rangle$ (thermal av) (Å)	$\langle\phi\rangle$ (thermal av) (deg)	Δ_O (cm^{-1})	e_ϵ (cm^{-1})	$\langle\rho\rangle$ (thermal av) (Å)	$\langle\phi\rangle$ (thermal av) (deg)
1.5	12000	650	0.38598	238.63				
10	12000	650	0.38598	238.63	12000	750	0.38426	237.70
30	12000	650	0.38598	238.63				
75	11980	625	0.38578	238.55				
100	11980	600	0.38547	238.47	12000	750	0.38400	237.67
150	11940	575	0.38457	238.34				
200	11810	480	0.38039	237.72	11800	700	0.38156	237.33
250	11480	290	0.34424	233.14	11700	550	0.37398	236.20
275					11650	525	0.36944	235.64
297	10600	190	0.28756	223.50	11500	500	0.36166	234.63

[a] Values for the remaining parameters (ref 8) are $A_1 = -900$ cm^{-1}, $A_2 = 33$ cm^{-1}, $A_3 = 0$, $\hbar\omega = 254$ cm^{-1}, $e_\theta = 700$ cm^{-1}, $B = 637$ cm^{-1}, $C = 2640$ cm^{-1}, $\zeta = 193.2$ cm^{-1}. Also shown are the thermally averaged expectation values of the nuclear coordinates, expressed in terms of the polar coordinates, ρ(av) (Å) and ϕ(av) (deg).
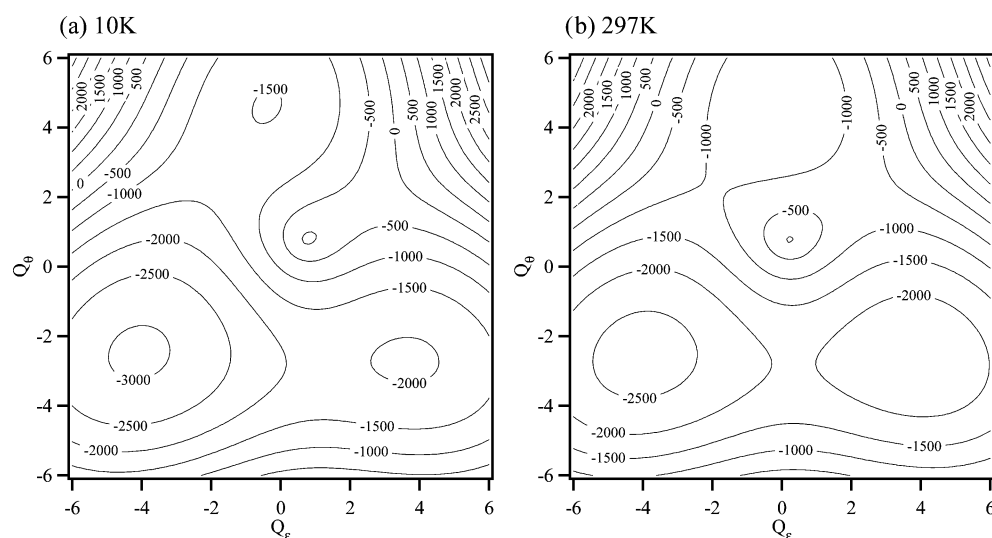

Figure 10. Contour plots of the E⊗e potential energy surface, perturbed by anisotropic strain, as calculated for $(ND_4)_2Cr(D_2O)_6(SO_4)_2$. Parameters common to both plots are $A_1 = -900$ cm^{-1}, $A_2 = 33$ cm^{-1}, $A_3 = 0$, $\hbar\omega = 254$ cm^{-1}, and $e_\theta = 700$ cm^{-1}. Plot (a) at 10 K was calculated with $e_\epsilon = 650$ cm^{-1}; plot (b) at 297 K was calculated with $e_\epsilon = 190$ cm^{-1}.

temperature to ascertain the values of the parameters, e_θ and e_ϵ, defining the anisotropic strain.

The convergence of the Cr−O(7) and Cr−O(8) bond lengths in the $(ND_4)_2Cr(D_2O)_6(SO_4)_2$ salt, at elevated temperatures, is indicative of the coexistence of different structural conformations of the $[Cr(D_2O)_6]^{2+}$ cation. With fixed values of e_θ and e_ϵ, the observed trend can be reproduced, but agreement with the experimental data is poor, as shown in Supporting Information. The fit is improved significantly if the e_ϵ parameter is allowed to vary with temperature, following the procedure used to model data for the $(ND_4)_2Cu(D_2O)_6(SO_4)_2$ salt.[60−62] In Figure 7, the experimental Cr−O bond lengths are shown along with those calculated using the strain parameters given in Table 5. At 10 K, the bond lengths may be reproduced with $e_\theta = 700$ cm^{-1} and $e_\epsilon = 650$ cm^{-1}; at 297 K, e_ϵ must be reduced to 190 cm^{-1}. The effect of the variation of the anisotropic strain on the Jahn−Teller energy surface is illustrated in Figures 10 and 11. Figure 10 shows contour plots of the perturbed E⊗e potential energy surface at 10 and 297 K. In Figure 11, the potential energy is plotted as a function of the angular coordinate, ϕ, following the path of minimum energy. Figure 12 shows the change in the strain vector, $\vec{s}$, as a function of temperature, which brings about the change in the form of the surface.

At 10 K, the strain can be represented as a vector, $\vec{s}$, of length, $\delta = 955$ cm^{-1}, and angle, $\varphi = 223°$, in the e_θ, e_ϵ coordinate frame (Figure 12). The potential well at $\phi \approx 240°$ (O_h) is lowered in energy relative to the other two and is also distorted, such that the minimum no longer lies at $\phi = 240°$ (Figure 10). The expectation value of the nuclear coordinates of the ground $S = 2$ manifold is now at $\phi = 238.63°$ (Table 5), equating to a small rhombic distortion in the equatorial plane. The consequence of decreasing e_ϵ, while keeping e_θ constant, is to change the magnitude and direction of $\vec{s}$ (Figure 12). Both δ and φ decrease steadily upon increasing temperature, reaching 725 cm^{-1} and $\varphi = 195°$ at 297 K. The change in both of these parameters leads to a pronounced reduction in the energy gap between the two lowest-lying wells upon increasing temperature, as seen in Figure 11. The thermal population of excited vibronic states, localized in the upper well, becomes significant above ∼200 K, giving rise to an *apparent* rapid convergence in the Cr−O(7) and Cr−O(8) bond lengths, when the space-averaged property is measured.

The INS experiments are a measure of the expectation values of the electronic coordinates in the thermally populated $S = 2$ manifolds. The spectra of $(ND_4)_2Cr(D_2O)_6(SO_4)_2$ can be reproduced directly from the eigenvalues and eigenfunctions of the
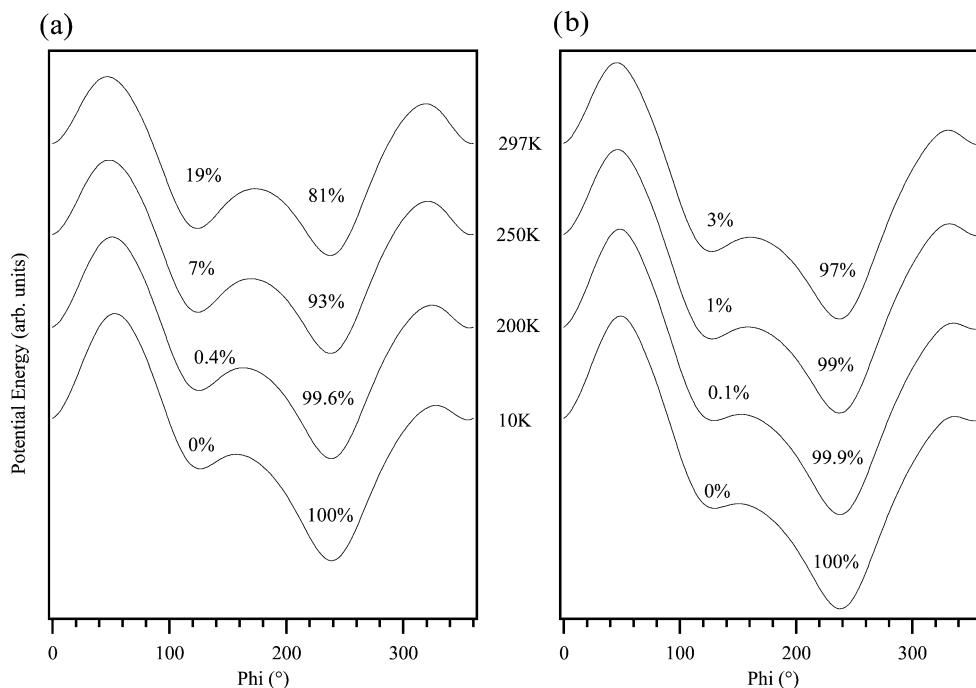
(a)

(b)

Figure 11. Variation of the potential energy as a function of the angle, Phi, along the path of minimum energy. Traces were calculated for different temperatures using the strain and vibronic Hamiltonian parameters listed in Table 5 for (a) $(ND_4)_2Cr(D_2O)_6(SO_4)_2$ and (b) $Rb_2Cr(D_2O)_6(SO_4)_2$. The relative Boltzmann populations of the two lowest potential minima are indicated above each trace.
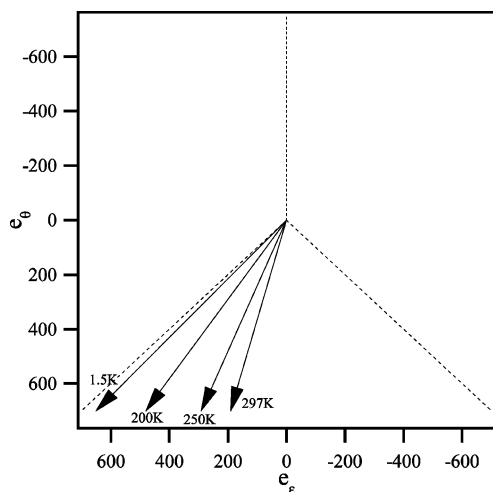

Figure 12. Plot of the strain vector as a function of temperature, derived from modeling the experimental data obtained for $(ND_4)_2Cr(D_2O)_6(SO_4)_2$. The broken lines indicate values of φ of 0, 120, and 240° in the e_θ, e_ϵ (cm⁻¹) coordinate space. A strain along these directions would give rise to a CrO_6 framework of strict D_{4h} symmetry.

vibronic Hamiltonian using the strain parameters obtained from modeling the bond lengths, the ligand-field parameters estimated from the optical spectra, and by setting ζ to 193.2 cm⁻¹. The theoretical spectra are shown in Figure 13 and are in good agreement with the experimental spectra presented in Figure 1. The value of ζ is of little significance as the Racah parameters could not be precisely defined from the optical spectra. In addition, the effective ^5E_g electronic basis, employed in the calculation, was formulated assuming O_h symmetry, whereas the $[Cr(D_2O)_6]^{2+}$ cation lies on a site of C_i symmetry in the Tutton's salts; discrepancies arising from the cubic approximation are absorbed into the ζ parameter. The INS data can also be modeled satisfactorily with an $S = 2$ spin Hamiltonian, and it is convenient to discuss the ground-state electronic structure
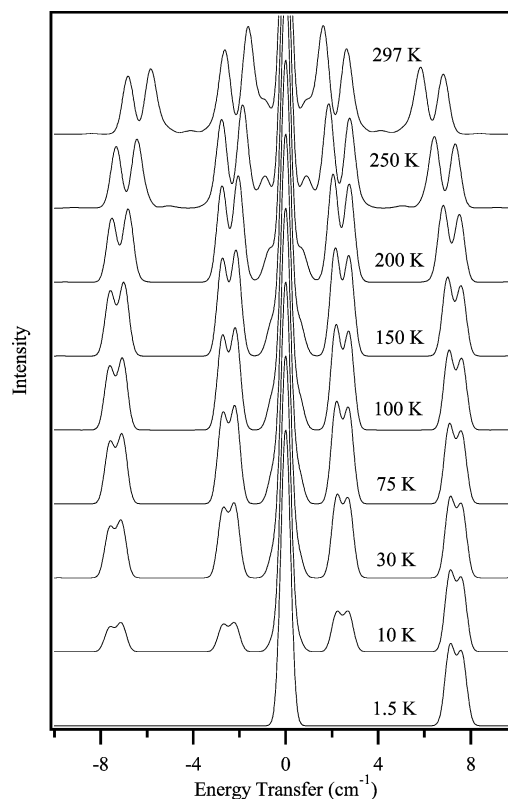

Figure 13. Theoretical INS spectra of $(ND_4)_2Cr(D_2O)_6(SO_4)_2$ between 1.5 and 297 K, calculated directly from the eigenfunctions and eigenvalues of the vibronic Hamiltonian using the following parameter set: $\hbar\omega = 254$, $B = 637$, $C = 2640$, $\zeta = 193.2$, $A_1 = -900$, $A_2 = 33$, $A_3 = 0$, and $e_\theta = 700$ cm⁻¹; values of Δ_O and e_ϵ were varied according to Table 5. All transitions were folded with a Gaussian line shape with a full width at half-height of 0.25 cm⁻¹.

of the $[Cr(D_2O)_6]^{2+}$ in terms of the zfs parameters. The decrease in the magnitude of the parameter D, shown in Figure 5, can be reproduced only by assuming that the ligand-field parameters

are temperature dependent. The optical spectra of $(ND_4)_2Cr$-$(D_2O)_6(SO_4)_2$ suggest a reduction in the energy difference between the ^5E_g (O_h) and $^5T_{2g}$ (O_h) terms, a quantity directly related to the ligand-field octahedral splitting parameter, Δ_O. Decreasing Δ_O upon increasing temperature, according to the values given in Table 5, while keeping B, C, and ζ constant, gives rise to a reduction in the zfs of the ground state, comparable to that found experimentally. The increase in the parameter, E, can be understood in terms of changes in the adiabatic potential energy surface as a rhombic distortion of the CrO_6 framework is concomitant with a rhombic component to the ligand-field. The change in the value of φ upon increasing temperature, depicted in Figure 12, results in the minima of the potential wells occurring at values of ϕ, deviating ever farther from the co-Kernel points of D_{4h} symmetry. Considering only the expectation values of the nuclear coordinates of the ground $S = 2$ manifold, ϕ decreases from $238.63°$ at 5 K to $237.17°$ at 297 K.

The values of D and E, determined from the EPR measurements, show notable deviations from those determined by INS. To explain these discrepancies, it is necessary to consider the effect of motional averaging on the observed EPR spectrum. Diagonalizing the vibronic Hamiltonian using the parameters listed in Table 5, we calculated a set of D and E values corresponding to a Boltzmann-weighted average of the spin-Hamiltonian parameters, assuming that the rate of intramolecular reorientations is fast on the EPR time scale but slow on the INS time scale, according to the procedure outlined in sections 3.2.2. and 3.2.3. Above ~200 K, the two sets of calculated values deviate significantly, in accordance with the trends suggested by the EPR and INS data, as shown in Figure 5.

The experimental quantities for the rubidium and cesium salts also vary with temperature, though not as strongly as for the ammonium salt. The parameters that best reproduce the crystallographic and spectroscopic data are given in Supporting Information. Compared to that in the ammonium salt, the decrease in the orthorhombic strain parameter, e_ϵ, with increasing temperature, is marginal. Consequently, there is little variation in the form of the potential energy surface, as shown for the rubidium salt in Figure 11b; at all temperatures, the thermally occupied states are strongly localized in the lowest energy potential well. In this instance, therefore, there is no difference in the spin-Hamiltonian parameters determined by the EPR and INS techniques.

The contrasting data obtained for the ammonium and rubidium Tutton's salts result primarily from differences in the strength and nature of the anisotropic strain transmitted via hydrogen-bonding, which is more pervasive in the ammonium salt. Two distinct models have been put forward to rationalize the variation in the parameter, e_ϵ, with temperature. In one model, a uniform lattice strain acts on every molecule, which changes with temperature;[60,61] another model assumes that cooperative interactions produce a range of strain values at higher temperatures, in which case, e_ϵ is an effective parameter, representing an average of strains experienced by complexes with different environments.[62]

6. Conclusion

The standard procedure for the characterization of high-spin d^4 complexes has been to interrelate low-temperature HFEPR with structural data often obtained only at room temperature. This work has shown that such an approach affords but a shallow understanding of the structure and bonding of the molecule. A variety of spectrocopic and crystallographic techniques should be employed over as wide a temperature range as possible to facilitate a rigorous definition of the vibronic structure. The application of both EPR and INS has been shown to be a particularly powerful probe of the dynamical Jahn−Teller effect as apparent inconsistencies in the spin-Hamiltonian parameters derived from these experiments are, in fact, a consequence of intramolecular reorientations of the molecule. The experimental data presented for the chromium(II) Tutton's salts set a new standard to which theoretical models should be compared and have been satisfactorily reproduced using the eigenvalues and eigenfunctions obtained from numerical diagonalization of a $^5E \otimes e$ vibronic Hamiltonian, perturbed by anisotropic strain.

Supporting Information Available: Tables of fractional coordinates, thermal parameters, unit cell parameters, selected interatomic bond lengths, as well as additional EPR spectra and theoretical calculations. This material is available free of charge via the Internet at http://pubs.acs.org.

JA046095C

(60) Hitchman, M. A.; Yablokov, Y. V.; Petrashen, V. E.; Augustyniak-Jablokov, M. A.; Stratemeier, H.; Riley, M. J.; Lukaszewicz, K.; Tomaszewski, P. E.; Pietraszko, A. *Inorg. Chem.* **2002**, *41*, 229.
(61) Marciniak, M.; Hoffmann, S. K.; Augustyniak, M. A.; Hilczer, W. *Phys. Status Solidi B* **1995**, *191*, 201.
(62) Hitchman, M. A.; Maaskant, W.; Plas, J.; Simmons, C. J.; Stratemeier, H. *J. Am. Chem. Soc.* **1999**, *121*, 1488.